Eulerian modeling of inertial and diffusional aerosol deposition in bent pipes

Frederix, E. M. A.; Kuczaj, A. K.; Nordlund, M.; Veldman, A. E. P.; Geurts, B. J.

Published in:
Computers & fluids

DOI:
10.1016/j.compfluid.2017.09.018

Publication date:
2017

Computers and Fluids 159 (2017) 217–231

Contents lists available at ScienceDirect

Computers and Fluids

journal homepage: www.elsevier.com/locate/compfluid

Eulerian modeling of inertial and diffusional aerosol deposition in bent pipes

E.M.A. Frederix[a,*], A.K. Kuczaj[d,a], M. Nordlund[d], A.E.P. Veldman[c,a], B.J. Geurts[a,b]

[a] Multiscale Modeling and Simulation, Faculty EEMCS, University of Twente, P.O. Box 217, Enschede 7500 AE, The Netherlands
[b] Anisotropic Turbulence, Fluid Dynamics Laboratory, Faculty of Applied Physics, Eindhoven University of Technology, P.O. Box 513, Eindhoven 5600 MB, The Netherlands
[c] Institute of Mathematics and Computing Science, University of Groningen, P.O. Box 407, Groningen 9700 AK, The Netherlands
[d] Philip Morris International R&D, Philip Morris Products S.A., Quai Jeanrenaud 5, Neuchatel CH-2000, Switzerland

ARTICLE INFO

Article history:
Received 19 August 2016
Revised 31 May 2017
Accepted 23 September 2017
Available online 25 September 2017

Keywords:
Aerosol
Deposition
Drift
Diffusion
Transport
Bent pipe
Droplet size distribution

ABSTRACT

This paper presents a sectional Eulerian aerosol model for size-dependent droplet deposition at walls of the domain, driven by both diffusion and inertia. The model is based on the internally mixed assumption and employs the formulation for compressible aerosols. It is validated in a bent pipe geometry against models and experimental and numerical data from literature. Good agreement is found in both the diffusion and inertial deposition regimes. To improve the overprediction of inertial deposition by a boundary treatment that adopts zero-gradient droplet wall velocity, we use a corrected wall velocity, based on an analytical solution of the droplet motion near the wall. In the bent pipe setting the corrected wall velocity is found to reduce the overprediction of deposition and is less sensitive to grid refinement. We also show that refining the computational mesh near the pipe wall improves the predicted deposition efficiency, significantly. Finally, we present a parameter study varying the Reynolds number and the bend curvature. The deposition efficiency curve is recorded for droplet diameters ranging from the nanometer scale to beyond the micrometer scale, which is a unique contribution of this paper. The complete size range is simulated in only one simulation, due to the sectional approach. In the diffusion-dominated regime an increase in Reynolds number leads to a gradual enhancement of deposition. In the inertial regime, where droplet drift dominates deposition, a much stronger dependence on the Reynolds number is found. The dependence of the deposition on the bend curvature is less pronounced. The results shown in this paper establish the role of Eulerian simulation in predicting deposition of aerosol droplets and are useful for understanding size-dependent aerosol deposition in other more complex confined geometries.

1. Introduction

Two of the main mechanisms of aerosol deposition are inertial impaction and diffusion [1]. Both processes are strongly size dependent; small aerosol droplets deposit due to high diffusivity, large droplets due to large momentum and intermediately-sized droplets deposit more scarcely. In a setting where the Reynolds number is sufficiently high so that gravitational settling becomes negligible, this leads to the well-known deposition efficiency curve which has a characteristic 'V' shape. This was observed in many kinds of geometry that involve aerosol deposition, e.g., in respiratory flow [2–4] or flow around an object [5,6]. The exact shape of this deposition curve characterizes the filtration efficiency of an object or geometry, and is very useful for understanding aerosol deposition.

A common way to study aerosol deposition is to consider aerosol flow through a bent pipe. The bent pipe geometry offers a simple setting in which the mechanisms behind aerosol deposition can be systematically studied. In fact, the bent pipe can be used as a highly idealized mouth–throat model to emulate aerosol droplet deposition in the human airways, see [7]. By studying the bent pipe a qualitative impression can be formed of both the flow and aerosol deposition patterns.

The bent pipe problem has been studied by many authors and therefore offers a reliable and well-understood point of reference. Earlier theoretical works studied particle trajectories in the bent pipe given an approximate flow field [8–10]. More recently, many

* Corresponding author.
E-mail address: e.m.a.frederix@utwente.nl (E.M.A. Frederix).

https://doi.org/10.1016/j.compfluid.2017.09.018

authors have published CFD simulations of particle deposition in bends using Lagrangian (e.g., [11–14]) or Eulerian methods (e.g., [15–20]). Others have studied aerosol deposition in pipe bends experimentally, e.g., [7,12,21,22]. The seminal work of Pui et al. [21] is key in the literature concerning bent pipe aerosol deposition efficiency and a clear source for validation. For example, Pilou et al. [15] found good agreement for Reynolds numbers $Re = 100$ and $Re = 1000$ and Vasquez et al. [20] found good agreement for $Re = 1000$ while an overprediction of the deposition efficiency for $Re = 100$ was observed.

Most bent pipe studies focused on the 'inertial deposition regime', looking at aerosol droplets or particles with a Stokes number typically larger than 0.01. For these droplets it is their inertia that leads to a collision with a geometry wall. However, as noted before, sufficiently small droplets may also deposit by diffusion. In fact, in many applications the aerosol droplet size is such that droplet diffusion and inertia are two important effects, e.g., see [2,23,24]. In this paper, we consider aerosol deposition in a bent pipe for droplet sizes ranging from the nanometer scale to beyond the micrometer scale.

Recently, we developed an Eulerian, sectional, internally-mixed aerosol model [25,26] capable of predicting the evolution of the droplet size distribution undergoing nucleation, condensation, evaporation and coagulation. We formulated a compressible model in which the mixture density is constituted by a number of chemical species, either present as vapor or in the form of liquid droplets. Building on that foundation, in this paper we extend this model to include droplet drift, diffusion and wall deposition. The main objective of this paper is to present the model and to validate our Eulerian approach against data from literature, in both the diffusion and the inertial regime. Moreover, we study how predictions depend on the chosen grid and boundary treatment for the droplet velocity.

The sectional Eulerian model retains a compressible formulation in which the mixture density is composed of both vapors and liquids, mitigating a passive scalar approach as is done in many other works, e.g., [15,23]. This couples the aerosol processes, such as droplet drift and diffusion but also nucleation and condensation (see [25,26]) to the transport equations for mass, momentum and energy. This may be relevant in cases where mixture compressibility is important, or where temperature changes are large. However, also in systems not exhibiting these features the compressible fluid framework is beneficial for obtaining general and accurate models as reliable constitutive relations can be formulated explicitly. In combination with a pressure-based approach [27] this combines consistency in the physical model with computational efficiency. We develop a scheme which, by construction, implements two constraint equations ensuring (1) that species mass fractions always add up to unity and (2) that the first moment of the size distribution is also reflected in the liquid mass concentration solution.

For large droplets we compare the predictions of our model against aforementioned experimental and numerical bent pipe studies. For small droplets we compare against the analytical straight pipe diffusional deposition model of Ingham [28]. In both regimes we find good agreement, provided sufficient spatial resolution of the solution is adopted.

In this paper we present a detailed numerical study of our model for droplet diffusion, drift and subsequent deposition. We study the two cases presented by Pui et al. [21], for Reynolds number $Re = 100$ and $Re = 1000$, on five different meshes in which we compare results obtained with or without grid refinement near the wall. We use two boundary treatments for the droplet velocity at the wall, i.e., a 'zero-gradient' boundary condition, keeping the droplet velocity from cell center to the wall constant, and a corrected boundary condition as proposed in [23], employing the analytical solution of the droplet equation of motion near the wall in a linearized flow field. The corrected boundary condition is shown to decrease the overestimation of the deposition efficiency, and generally is less resolution sensitive. We show that the wall grid-refined meshes improve the predictions of the deposition curve significantly. We also present a parameter study for the dependence of the deposition efficiency on the Reynolds number and the bend curvature. An enhancement of both diffusion and inertial deposition is shown for increasing Reynolds number whereas the dependence on the bend curvature is small.

In the model validation presented in this paper, we consider aerosol deposition in a bent pipe for droplet sizes ranging from the nanometer scale to beyond the micrometer scale. This enormous size-range is the unique feature of our model: within one formulation the corresponding deposition efficiency curve spanning the complete size domain is predicted. Moreover, the sectional formulation spanning many decades in droplet sizes allows for a straight-forward extension to include aerosol processes such as nucleation, condensation, evaporation and coagulation or breakup, as was done before (see [25,26,29]). The combination of these capabilities forms a unique and quite complete aerosol model.

The layout of this paper is as follows. In Section 2 we will, starting from the equation of motion for the droplet size distribution, construct a set of equations describing a compressible 'internally mixed' [30] multi-species aerosol in an Eulerian way, including a new drift flux term. Next, in Section 3, we will adopt a finite volume method and discretize the transport equations accordingly. Again, special attention is paid to retaining the consistency among the equations, also in their discrete forms. Two boundary treatments for the droplet velocity at the wall are discussed. In Section 4.1 we present the bend pipe geometry and in Section 4.2 the fluid velocity solution is validated against data from [15]. Next, in Section 4.3 the grid sensitivity of the solution is shown using both the corrected and uncorrected wall treatments. We validate the inertial and diffusion regime of the deposition curve in Sections 4.4 and 4.5, respectively. Finally, in Section 4.6 we present a parameter study.

2. An internally mixed Eulerian aerosol model with droplet drift and diffusion

In this section, we will discuss the 'internally mixed' multi-species Eulerian model that we adopt for the description of the evolution of an aerosol mixture. Subsequently, we extend it to incorporate drift flux and diffusion terms, based on a size-dependent drift velocity and Brownian diffusivity. The considerations taken in arriving at the drift flux model will be discussed here.

2.1. Mass and droplet concentration transport equations

Let us consider a volume in which we have $\mathcal{N}$ species, present as vapor and liquid, where the liquid phase is contained in dispersed droplets. With respect to the total mass in this volume, the jth species has a mass fraction Y_j present as vapor and Z_j present as liquid. By definition, we have

$$\sum_j (Y_j + Z_j) = 1. \tag{1}$$

Vapors are assumed to be ideal gases and liquids are assumed to be incompressible. Using Amagat's law [31], the mixture density ρ can be related to the species-specific vapor compressibility ratios, species-specific liquid densities, pressure and temperature, giving an equation of state in the form of

$$\rho = \psi(p, T)\, p, \tag{2}$$

with $\psi(p, T)$ the 'effective' compressibility ratio. Following Frederix et al. [26], we introduce

$$\psi^{-1}(p,T) = \sum_j \frac{Y_j}{\psi_j^\star(T)} + p\sum_j \frac{Z_j}{\rho_j^\star(T)}, \tag{3}$$

with $\psi_j^\star(T)$ the vapor compressibility ratio and $\rho_j^\star(T)$ the liquid density, both for j-species pure constituents of species j only. These quantities are both temperature-dependent. Since (2) together with (3) is based on Amagat's law it has the implication that volume is an extensive quantity, meaning that the specific volumes are independent of mixture composition.

For the evolution of the mixture density, assuming that droplets and vapors are moving with the same velocity $\mathbf{u}$, the continuity equation holds:

$$\partial_t \rho + \nabla\cdot(\rho\mathbf{u}) = 0 \tag{4}$$

This can be expanded for all species in both phases, giving the transport equations for the jth species vapor and liquid mass concentrations:

$$\partial_t(\rho Y_j) + \nabla\cdot(\rho Y_j\mathbf{u}) = 0 \tag{5a}$$

$$\partial_t(\rho Z_j) + \nabla\cdot(\rho Z_j\mathbf{u}) = 0. \tag{5b}$$

Eq. (5b) provides information about the evolution of the liquid mass concentration for each species, under the assumption that the overall liquid motion is equal to the mixture motion, requiring the liquid droplets to be sufficiently small. We may readily relax this assumption by incorporating the droplet size distribution instead. In fact, the liquid mass is present in the form of many dispersed droplets, suggesting that the liquid phase may also be described by the droplet size distribution $n(s, \mathbf{x}, t)(s, \mathbf{x}, t)$, where s is the mass of a droplet. This is useful for the description of processes that depend on the size of a droplet, such as droplet drift or diffusion. For the evolution of the droplet size distribution, we introduce the General Dynamic Equation (GDE), see [26,30]. Extending the model as given by (5) to include droplet motion that differs from the mixture motion, we replace the mixture velocity $\mathbf{u}$ in the GDE with the size-dependent droplet velocity $\mathbf{v}(s)$, which is written as

$$\mathbf{v}(s) = \mathbf{u} + \mathbf{u}^\ell(s), \tag{6}$$

where $\mathbf{u}^\ell(s)$ is the liquid drift velocity of an s-sized droplet with respect to the motion of the carrier gas, $\mathbf{u}$. The corresponding GDE for $n(s, \mathbf{x}, t)(s, \mathbf{x}, t)$ can be expressed as

$$\begin{aligned}&\partial_t n(s,\mathbf{x},t)(s,\mathbf{x},t) + \nabla\cdot(\mathbf{u}(s,\mathbf{x},t)) + \nabla\cdot(\mathbf{u}^\ell(s)n(s,\mathbf{x},t)(s,\mathbf{x},t))\\ &\quad = \nabla\cdot(\mathbb{D}(s)\nabla n(s,\mathbf{x},t)(s,\mathbf{x},t)),\end{aligned} \tag{7}$$

where $\mathbb{D}(s)$ is the droplet diffusivity, to be defined momentarily. Eq. (7) contains two convective fluxes: one with respect to $\mathbf{u}$ and a second one with respect to $\mathbf{u}^\ell(s)$. The latter flux term, as well as the right-hand side diffusion term, expresses that droplets can move independently of the mixture. This extension requires to also modify (5) to adequately reflect these additional dynamics. Moreover, the continuity equation reflecting mass conservation must be augmented with an extra conservative divergence term incorporating the local appearance or removal of droplets by drift. We turn to this task next.

Let us first consider the droplet size distribution for an internally mixed aerosol, as was discussed in [26]. The first moment of this size distribution is required to be equal to the total mass concentration of droplets, i.e.,

$$\rho Z = \int_0^\infty sn(s,\mathbf{x},t)(s,\mathbf{x},t)\,\mathrm{d}s, \tag{8}$$

where $Z = \sum_j Z_j$. This equation implies that ρZ and $n(s, \mathbf{x}, t)(s, \mathbf{x}, t)$ are mutually consistent and it allows us to relate the droplet drift to the rate of change of the total droplet mass concentration. By multiplying (7) by s, and then taking the integral from 0 to ∞ in s, we find

$$\partial_t(\rho Z) + \nabla\cdot(\rho\mathbf{u}Z) + \nabla\cdot(Z^{-1}\mathbf{f}Z) = 0, \tag{9}$$

where we have introduced the product $Z^{-1}Z$ (which is unity) into the drift divergence terms, for later use, and where

$$\mathbf{f} = \mathbf{f}^{\text{drift}} - \mathbf{f}^{diff} \tag{10}$$

and

$$\mathbf{f}^{\text{drift}} = \int_0^\infty s\mathbf{u}^\ell(s)n(s,\mathbf{x},t)(s,\mathbf{x},t)\,\mathrm{d}s \tag{11a}$$

$$\mathbf{f}^{\text{diff}} = \int_0^\infty s\mathbb{D}(s)\nabla n(s,\mathbf{x},t)(s,\mathbf{x},t)\,\mathrm{d}s \tag{11b}$$

The flux $\mathbf{f}$ can be considered as the total flux of liquid concentration moving away from the mixture motion due to drift or diffusion. Recalling that $Z = \sum_j Z_j$ and introducing this in (9), we can expand (9) in j-space as

$$\partial_t(\rho Z_j) + \nabla\cdot(\rho\mathbf{u}Z_j) + \nabla\cdot(Z^{-1}\mathbf{f}Z_j) = 0, \tag{12}$$

Eq. (12) is consistent with (9). In the case of no drift and no diffusion, the third term of the left-hand side is zero and we recover the original transport equation for Z_j in which liquid is convected by $\mathbf{u}$ only, Eq. (5b). Satisfying separately (12) for each j automatically satisfies (9) as well. The product $Z^{-1}Z_j$ as found in (12) can be considered as the mass fraction of liquid species j with respect to the total *liquid* mass concentration. Therefore, the flux $Z^{-1}\mathbf{f}Z_j$ in (12) can be interpreted as the total flux of *j-species* liquid concentration drifting away from the mixture.

The transport equation of j-species liquid mass concentration, Eq. (12), is fully consistent with that of the size distribution, Eq. (7), imposed by the consistency relation (8). We set out to formulate a new augmented continuity equation, but for this we must still consider the transport of vapor concentration, ρY_j. From a physical point of view we assume that when droplets drift, the volume they 'vacate' is replenished by a counterflow of vapor mixture of equal volume. In this way, given our compressible mixture equation of state (2) and (3) which is based on the idea that volume is an extensive quantity, pressure remains uniform. We now introduce a compensating vapor drift term, to account for this counterflow. Without the explicit compensation of volume, the pressure would locally change due to droplet drift, which leads to a pressure gradient-induced flow in $\mathbf{u}$. This would affect the complete mixture. Let ρ^v denote the local mean vapor density and ρ^ℓ the local mean liquid density. Then the total vapor mass concentration drift flux, compensating for the droplet mass drift flux, is given by

$$\mathbf{h} = \gamma\mathbf{f}, \tag{13}$$

with $\gamma = \rho^v/\rho^\ell$, and the j-species-specific contribution is taken as $Y^{-1}\mathbf{h}Y_j$, i.e., weighed with the relative contribution of species j to the total local vapor mass, where $Y = \sum_j Y_j$. Subtracting this compensating flux (it is in opposite direction relative to the liquid flux) from the left-hand side of Eq. (5a), we find

$$\partial_t(\rho Y_j) + \nabla\cdot(\rho\mathbf{u}Y_j) - \nabla\cdot(Y^{-1}\mathbf{h}Y_j) = 0 \tag{14}$$

Since we have chosen to compensate the supply or removal of volume as a result of droplet drift by an equal vapor mixture volume, inevitably the local density will decrease when droplets are moving away, because generally $\gamma \ll 1$. This perturbation of density should be accounted for in the continuity equation, and in the corresponding pressure equation. By adding (12)–(14), and summing over j we find:

$$\partial_t\rho + \nabla\cdot(\rho\mathbf{u}) + \nabla\cdot[\mathbf{f}(1-\gamma)] = 0. \tag{15}$$

When $\gamma = 1$, the compensating vapor volume has the same mass as the drifting droplets, leading to zero net mass change by drift. Indeed, in that case the third term in Eq. (15) becomes zero, reducing it to the usual continuity equation.

To summarize, we now established a set of transport equations for mass concentration, Eq. (15), liquid and vapor species-specific mass concentrations, Eqs. (12) and (14), and for the droplet size distribution, Eq. (7), for the compressible Eulerian description of a multi-species internally mixed aerosol. Consistency among these equations is enforced by the mass fraction unity constraint, Eq. (1), and the first moment mass concentration constraint, Eq. (8).

2.2. Drift velocity model

In the previous section we introduced the droplet velocity $\mathbf{v}(s)$, Eq. (6), differing from the mixture velocity $\mathbf{u}$ by a drift velocity. We must formulate a model for the description of $\mathbf{v}(s)$, as a function of the droplet size. Generally, within the drift flux framework there are two popular choices to establish such a model. First, a so-called local equilibrium approximation framework (see [6,32]) may be adopted in which $\mathbf{v}(s)$ may be found using an algebraic relation which stems from the droplet equation of motion in which the acceleration of the droplet is assumed to be equal to the local carrier fluid acceleration. Second, we may apply the complete equation of motion of a droplet retaining the acceleration of the droplet. In this paper we adopt this 'full model'.

Following Manninen et al. [32] the motion of a single s-sized droplet can, in a Lagrangian way, be described by Newton's second law of motion, i.e.,

$$z\,\mathrm{d}_t\mathbf{v} = \mathbf{f}_D + \mathbf{f}_G, \tag{16}$$

where we only include the drag force $\mathbf{f}_D$ and the gravitational force $\mathbf{f}_G$ as the dominant contributions for droplets with $\gamma \ll 1$ [33]. The drag force can be written as [34]

$$\mathbf{f}_D = -\frac{1}{2}A_d\rho^\ell C_D|\mathbf{u}^\ell|\mathbf{u}^\ell, \tag{17}$$

with cross-sectional droplet area A_d and drag coefficient C_D. The gravity force acting on the droplet is given by

$$\mathbf{f}_G = (\rho^\ell - \rho^v)V_d\mathbf{g}, \tag{18}$$

with droplet volume V_d and gravitational acceleration vector $\mathbf{g}$. C_D is a function of the droplet Reynolds number, given by

$$Re_d = \frac{d\rho^v|\mathbf{u}^\ell|}{\mu}, \tag{19}$$

with droplet diameter d and vapor mixture viscosity μ. For sufficiently low Re_d (see [34] for more detail), C_D takes the form of Stokes drag,

$$C_{D,St} = \frac{24}{Re_d}. \tag{20}$$

Eq. (16) constitutes a partial differential equation (PDE) in the Eulerian context. We may express the material time derivative as:

$$\mathrm{d}_t\mathbf{v} = \partial_t\mathbf{v} + (\mathbf{v}\cdot\nabla)\mathbf{v}. \tag{21}$$

Under the assumption that Stokes drag applies, the PDE for $\mathbf{v}$, given a mass s and corresponding diameter d, becomes

$$\partial_t\mathbf{v} + (\mathbf{v}\cdot\nabla)\mathbf{v} = -\frac{1}{\tau}(\mathbf{v}-\mathbf{u}) + (1-\gamma)\mathbf{g}, \tag{22}$$

with the droplet relaxation time

$$\tau = \frac{\rho^\ell d^2}{18\mu}. \tag{23}$$

Eq. (22) can be solved numerically for $\mathbf{v}$. Note that $\mathbf{v} = \mathbf{v}(s, \mathbf{x}, t)$, i.e., a Eulerian velocity field expressing the time-, space- and size-dependent droplet velocity.

2.3. The Stokes–Einstein model for Brownian diffusion

The diffusive flux $\mathbf{f}^{\mathrm{diff}}$ depends on the size-dependent diffusivity $\mathbb{D}(s)$. This diffusivity also appears in the diffusion term in the GDE. We adopt the Stokes–Einstein equation, providing a model for the Brownian diffusivity of a spherical body. It implies [1]

$$\mathbb{D}(s) = \frac{k_B T C_c}{3\pi\mu d}, \tag{24}$$

with k_B the Boltzmann constant, temperature T, Cunningham correction factor C_c, mixture viscosity μ and droplet diameter $d = d(s)$ related to the droplet mass s as

$$s = \tfrac{1}{6}\rho^\ell\pi d^3. \tag{25}$$

We compute the Cunningham correction factor, accounting for surface slip of small droplets, as [1]

$$C_c = 1 + \frac{\lambda}{d}\left[2.34 + 1.05\exp\left(-0.39\frac{d}{\lambda}\right)\right], \tag{26}$$

with λ the mean free path of the vapor mixture. For $d \gg \lambda$ this function becomes unity. For $d \ll \lambda$, C_c becomes proportional to d^{-1}, making the diffusivity (24) increase quadratically as d becomes smaller.

3. A sectional method retaining mass fractions and liquid mass

In the previous section, we motivated a set of equations for the compressible Eulerian description of an internally mixed multi-species aerosol. At the analytical level we showed that two consistency relations, one for the mass fractions (1) and one for the first moment of the droplet size distribution (8), were satisfied. In this section, we will introduce the sectional formulation to approximate a solution for the set of equations. Furthermore, at the discrete level we develop our method such that the two consistency relations, (1) and (8), are satisfied by construction.

3.1. The sectional formulation

Following Frederix et al. [25], we approximate the continuous size distribution function $n(s, \mathbf{x}, t)(s, \mathbf{x}, t)$ by a sectional formulation, in which droplets are divided in $\mathcal{P}$ so-called 'sections' labeled by their size s_i. Mathematically, $n(s, \mathbf{x}, t)(s, \mathbf{x}, t)$ is represented by

$$n(s, \mathbf{x}, t)(s, \mathbf{x}, t) = \rho\sum_i M_i\delta(s - s_i), \tag{27}$$

where $N_i = \rho M_i$ is the total number of droplets per unit volume having size s_i, i.e.,

$$\rho M_i = \int_{y_i}^{y_{i+1}} n(s, \mathbf{x}, t)(s, \mathbf{x}, t)\,\mathrm{d}s, \tag{28}$$

where y_i and y_{i+1} are the lower and upper boundary of section i. The formulation (27) implies that, with $\delta(s - s_i)$ having as unit one over mass and ρM_i number per unit volume, the size distribution has unit number per unit mass per unit volume.

By taking the integral over the interval $[y_i, y_{i+1}]$ of (7), and using (28), we find

$$\partial_t(\rho M_i) + \nabla\cdot(\rho\mathbf{u}M_i) + \nabla\cdot(\rho\mathbf{u}_i^\ell M_i) = 0, \tag{29}$$

where the drift velocity $\mathbf{u}_i^\ell = \mathbf{u}^\ell(s_i)$ is only evaluated at s_i due to the Dirac delta function representation of $n(s, \mathbf{x}, t)(s, \mathbf{x}, t)$ in (27). In terms of the sectional discretization the consistency relation (8) becomes

$$Z = \sum_i s_i M_i. \tag{30}$$

3.2. Finite volume discretization

OpenFOAM® offers a cell-centered collocated finite volume (FV) framework, in which we solve our system of equations. A detailed analysis of the integration of the Pressure-Implicit with Splitting of Operators PISO method in OpenFOAMwas presented in [27] for a two-moment description of an aerosol, and extended to a sectional model in [26]. In this framework, next, we include aerosol droplet drift. In the finite-volume method we consider a computational volume V with F faces, labeled by face index $1 \leq f \leq F$ and $\mathbf{A}_f$ the outward normal face vector with $|\mathbf{A}_f| = A_f$, i.e., the surface area of face f. Integrating (29) over the volume V, we find, approximating ρM_i as constant in V,

$$\partial_t(\rho M_i) + \mathcal{D}\left(\phi_f M_{i,f}\right) + \mathcal{D}\left(\phi^{\ell}_{i,f} M_{i,f}\right) = 0, \tag{31}$$

with fluxes

$$\phi_f = (\rho \mathbf{u})_f \cdot \mathbf{A}_f, \qquad \phi^{\text{drift}}_{i,f} = (\rho \mathbf{u}^{\ell}_i)_f \cdot \mathbf{A}_f \qquad \text{and}$$
$$\phi^{\text{diff}}_{i,f} = \mathbb{D}_{i,f} \nabla_f(\rho M_i) \cdot \mathbf{A}_f \tag{32}$$

with

$$\phi^{\ell}_{i,f} = \phi^{\text{drift}}_{i,f} - \phi^{\text{diff}}_{i,f} \tag{33}$$

and $M_{i,f} = (M_i)_f$, where $(\cdot)_f$ denotes interpolation to the face f, which we address momentarily. Also, in (32) there appears a term $\nabla_f(\rho M_i)$. This is the numerical representation of the gradient of ρM_i at face f. Note that this is generally different than $(\nabla(\rho M_i))_f$, i.e., the gradient of ρM_i computed at cell centers and only then interpolated to face f. Finally, in (31) we adopt the notation

$$\mathcal{D}\left(a_f\right) = \frac{1}{V}\sum_f a_f, \tag{34}$$

summing a_f over the faces f enclosing V. What remains is the discretization of the time derivative. We illustrate the remaining part of the development of our method by adopting the notationally compact implicit Euler scheme. We stress, however, that our approach remains applicable to any other time discretization scheme. Using the implicit Euler scheme, (31) may be time integrated from discrete time t^m at time level m to $t^{m+1} = t^m + \Delta t$ at time level $m+1$, as

$$\frac{(\rho M_i)^{m+1} - (\rho M_i)^m}{\Delta t} = -\mathcal{D}\left(\phi_f M_{i,f}\right)^{m+1} - \mathcal{D}\left(\phi^{\ell}_{i,f} M_{i,f}\right)^{m+1}. \tag{35}$$

This equation can be solved using the compressible PISO algorithm, as shown in [26,27]. The choice of interpolation scheme for the computation of $M_{i,f}$ is essential for the preservation of positivity of M_i. For example, the linear interpolation scheme is known to produce oscillations near sharp gradients; it is not monotonicity preserving. The upwind scheme, on the other hand, takes $M_{i,f}$ equal to M_i coming from the upwind direction, where the upwind direction is determined by the sign of the flux. The upwind scheme is TVD (Total Variation Diminishing). TVD schemes were shown to have the monotonicity property, i.e., the number of local extrema in the solution does not increase and local minima are nondecreasing and local maxima are nonincreasing [35]. This also means that when starting with a positive solution, a TVD scheme preserves positivity.

Generally, a TVD scheme determines its interpolation weights based on a limiter function. This limiter, in turn, is a function of the transported solution variable itself, as well as the face flux. In the case of (35), both divergence terms may be easily combined into one flux, $\phi_f + \phi^{\ell}_{i,f}$, on which the limiter can be based. For now, we leave the choice of interpolation scheme for $M_{i,f}$ undetermined (this choice will be addressed in Section 3.4), but assume that an appropriate interpolation is used that guarantees positivity of M_i^{m+1}.

The set of $\mathcal{P}$ Eq. (35) forms the discrete counterpart of the droplet size distribution transport Eq. (7). While for (7) we then enforced the analytical constraint (8) to find the consistent transport equation for Z, we will now follow a similar route for the numerical model starting from (35), and applying the discrete counterpart of (8), i.e., condition (30), to the transport equation for M_i. Multiplying (35) by s_i and summing over i, we find

$$\frac{(\rho Z)^{m+1} - (\rho Z)^m}{\Delta t} = -\mathcal{D}\left(\phi_f Z_f\right)^{m+1} - \mathcal{D}\left(Z_f^{-1}\phi^{\ell}_f Z_f\right)^{m+1} + \mathcal{J}^{m+1}, \tag{36}$$

where

$$\phi^{\ell}_f = \sum_i s_i \phi^{\ell}_{i,f} M_{i,f} \tag{37}$$

By following the same steps as in Section 2, but now at the discrete level, we may guarantee that the first moment consistency relation as expressed by (8) also holds discretely. Following this strategy, we expand (36) in j-space, which gives

$$\frac{(\rho Z_j)^{m+1} - (\rho Z_j)^m}{\Delta t} = -\mathcal{D}\left(\phi_f Z_{j,f}\right)^{m+1} - \mathcal{D}\left(Z_f^{-1}\phi^{\ell}_f Z_{j,f}\right)^{m+1}. \tag{38}$$

To ensure that this equation is consistent with (36) in the sense that summing (38) over j yields (36), we require that

$$Z_f = \sum_j Z_{j,f}. \tag{39}$$

This relation has an important numerical consequence, i.e., it implies that Z_f must be computed from the individual $Z_{j,f}$ interpolants, and not by first computing Z at cell centers and then interpolating this to the faces. While at high spatial resolutions the differences between $\Sigma_j Z_{j,f}$ and $(\Sigma_j Z_j)_f$ may be small, we adhere to the alternative definition of Z at the faces, following (39).

For convenience of implementation, we combine both convective terms in (38) into a single one, containing one flux on which the interpolation scheme can be based. This gives

$$\frac{(\rho Z_j)^{m+1} - (\rho Z_j)^m}{\Delta t} = -\mathcal{D}\left(\left[\phi_f + Z_f^{-1}\phi^{\ell}_f\right] Z_{j,f}\right)^{m+1}. \tag{40}$$

The term between square brackets on the right-hand side forms the flux with which Z_j is transported at face f. At the level of implementation, a difficulty with this form is that the flux contains Z_f^{-1}, which is undefined for $Z_f \to 0$. For numerical stability, the following form, where we multiply the flux by Z_f and divide $Z_{j,f}$ by Z_f, improves this:

$$\frac{(\rho Z_j)^{m+1} - (\rho Z_j)^m}{\Delta t} = -\mathcal{D}\left(\left[\phi_f \tilde{Z}_f + \phi^{\ell}_f\right] \frac{Z_{j,f}}{Z_f + \epsilon}\right)^{m+1}, \tag{41}$$

where the term between the square brackets is the total flux on which the interpolation scheme used for $Z_{j,f}$ and Z_f is based. This form has three consequences:

1. The number ϵ is a very small number. In case of $Z_f = 0$ as computed according to (39), the introduction of ϵ prevents division by zero. For $Z_f \to 0$, which, due to positivity, also implies that $Z_{j,f} \to 0$ for all j, the term $Z_{j,f}/(Z_f + \epsilon)$ also goes to zero; no liquid is present and no liquid is convected.
2. The convected scalar becomes $Z_f^{-1} Z_{j,f}$, which is non-linear in Z_j. We compute it explicitly, based on the latest iterative solution in the PISO algorithm, see [27].
3. Inside the flux there appears a Z_f which received an additional tilde in its notation. The reason for this is that $\tilde{Z}_f$ inside the flux cannot be computed from a limiter interpolation scheme which is based on the flux, as this Z_f is part of the flux itself. We should therefore choose a different form for this Z_f,

and therefore denote it as $\tilde{Z}_f$, indicating this. Due to the first moment consistency relation (30) we can compute $\tilde{Z}_f$ as

$$\tilde{Z}_f = \sum_i s_i M_{i,f}, \tag{42}$$

where each $M_{i,f}$ is computed by a TVD interpolation scheme.

Eq. (41) is the discrete equivalent of (12). By the same token, we can discretize the Y_j-Eq. (14) in an analogous way:

$$\frac{(\rho Y_j)^{m+1} - (\rho Y_j)^m}{\Delta t} = -\mathcal{D}\left(\left[\phi_f \tilde{Y}_f - \gamma \phi_f^\ell \right] \frac{Y_{j,f}}{Y_f + \epsilon} \right)^{m+1}, \tag{43}$$

where, as before, we have introduced ϵ for robustness. The term in the square brackets in the right-hand side is identified as the flux with which $Y_{j,f}/Y_f$ is convected. Also, we introduced $\tilde{Y}_f$ for which we derive an expression next.

Adding (41) and (43) to each other and summing the result over j gives the discrete form of the continuity Eq. (15), i.e.,

$$\frac{\rho^{m+1}(Y+Z)^{m+1} - \rho^m (Y+Z)^m}{\Delta t} = -\mathcal{D}\left(\phi_f \left[\tilde{Y}_f + \tilde{Z}_f \right] + \phi_f^\ell [1-\gamma] \right)^{m+1}, \tag{44}$$

provided that when summing (43) over j we have

$$\frac{\sum_j Y_{j,f}}{Y_f} = 1, \tag{45}$$

which is analogous to (39). After comparison of this discrete form of the continuity equation with its exact counterpart, (15), it becomes clear that we must require $\tilde{Y}_f + \tilde{Z}_f = 1$. To guarantee this, we compute $\tilde{Y}_f$ as

$$\tilde{Y}_f = 1 - \tilde{Z}_f = 1 - \sum_i z_i M_{i,f}. \tag{46}$$

The final form of the discrete density equation becomes

$$\frac{\rho^{m+1} - \rho^m}{\Delta t} = -\mathcal{D}\left(\phi_f + \phi_f^\ell [1-\gamma] \right)^{m+1}. \tag{47}$$

3.3. Deposition boundary treatment

When we use a no-slip boundary condition for the mixture velocity $\mathbf{u}$ then $\mathbf{u}$ is zero at the wall. The only two mechanisms allowing for droplet deposition on such walls are then, see Eq. (7), a non-zero drift velocity $\mathbf{u}^\ell(s)$, or a non-zero gradient of $n(s, \mathbf{x}, t)$ perpendicular to the wall, i.e., $\nabla n(s, \mathbf{x}, t) \cdot \mathbf{n}$ with $\mathbf{n}$ the general wall normal. At the discrete level, this translates into saying that $\phi_{i,f}^{\text{drift}} \neq 0$ to enable inertial deposition or $\phi_{i,f}^{\text{diff}} \neq 0$ to enable diffusional deposition, with f a face at the wall, see Eq. (32). We discuss these contributions next.

3.3.1. Inertial deposition

First, we consider inertial deposition. We consider a computational volume V located next to a wall with cell center position $\mathbf{x}_c$ and the face center at the wall located at $\mathbf{x}_f$, see Fig. 1 (left). The cell-outward unit normal of the wall face f is defined as

$$\mathbf{n}_f = \frac{\mathbf{A}_f}{A_f}, \tag{48}$$

and is shown in Fig. 1 (left). At the cell center we have a fluid velocity $\mathbf{u}$ and ith section droplet velocity $\mathbf{v}_i = \mathbf{v}(s_i)$. For very small droplets these two vectors become identical, and the drift velocity, i.e., $\mathbf{u}_i^\ell = \mathbf{v}_i - \mathbf{u}$ tends towards zero. Given the no-slip boundary condition for $\mathbf{u}$ at the wall, the droplet velocity at $\mathbf{x}_c$, for very small droplets, will also tend to zero as the computational grid is refined. We now assume that droplets maintain their velocity $\mathbf{v}_i$ close to the wall. This leads to the following *uncorrected deposition boundary condition*:

$$\text{BC}(\mathbf{v}_i) \text{ at the wall } \rightarrow \begin{cases} \nabla \mathbf{v}_i \cdot \mathbf{n} = 0, & \text{if } \mathbf{v}_i \cdot \mathbf{n} > 0 \\ \mathbf{v}_i = 0, & \text{otherwise} \end{cases} \tag{49a}$$

$$\text{BC}(n(s, \mathbf{x}, t)) \text{ at the wall } \rightarrow \nabla n(s, \mathbf{x}, t) \cdot \mathbf{n} = 0, \tag{49b}$$

which, for the drift velocity, is a mixed Dirichlet–Neumann boundary condition based on the condition $\mathbf{v}_i \cdot \mathbf{n} > 0$. If this condition is satisfied then the droplets close to the wall have a velocity pointing into the wall, and we set the droplet velocity *at the wall* to be equal to this velocity (i.e., the face-normal gradient of $\mathbf{v}_i$ is zero). If this condition is not satisfied, we set the droplet velocity at the wall to zero. The boundary condition for $n(s, \mathbf{x}, t)$ is of type Neumann, enforcing a zero gradient solution perpendicular to the wall. At the discrete level we implement the uncorrected deposition boundary condition as follows:

$$\mathbf{v}_{i,f} = \max(\mathbf{v}_{i,c} \cdot \mathbf{n}_f, 0) \mathbf{n}_f \tag{50a}$$

$$M_{i,f} = M_{i,c} \tag{50b}$$

$$\rho_f = \rho_c \tag{50c}$$

where subscript $(\cdot)_c$ denotes the cell centered value corresponding the control volume of which f is a face. Eq. (50a) sets $\mathbf{v}_{i,f}$ equal to the face-normal component of $\mathbf{v}_{i,c}$ if this component is positive, or otherwise to zero. Note that (50a) always sets a vector at face f inline with $\mathbf{n}_f$, discarding the components of $\mathbf{v}_c$ orthogonal to the face normal. This can be done as the drift droplet flux, expressed by Eq. (11), contains the inner product with $\mathbf{A}_f$, making only the wall-normal component of $\mathbf{v}$ relevant.

The uncorrected deposition boundary condition can lead to a significant overprediction of the droplet velocity at the wall [23]. In practice, as droplets travel from $\mathbf{x}_c$ to $\mathbf{x}_f$, they decelerate. Longest and Oldham [23] proposed a *corrected deposition boundary treatment*, employing the analytical solution of the droplet trajectory in between cell center and face center, assuming a linear decrease of the wall-normal fluid velocity to zero at the wall. Following their work, the equation of motion for the wall-normal velocity of a droplet in section i, undergoing only Stokes drag, is given by [34]

$$\mathrm{d}_t v_{i,f} = \tau^{-1} (u_f - v_{i,f}), \tag{51}$$

where $v_{i,f} = \mathbf{v}_i \cdot \mathbf{n}_f$, $u_f = \mathbf{u} \cdot \mathbf{n}_f$ and

$$\tau = \frac{\rho^\ell d^2 C_c}{18 \mu} \tag{52}$$

the droplet relaxation time. The mixture velocity, at the interval $[\mathbf{x}_c, \mathbf{x}_f]$, can be assumed to linearly decrease to zero, i.e.,

$$u = -\frac{x}{\delta_f} u_c, \tag{53}$$

with $x = (\mathbf{x} - \mathbf{x}_f) \cdot \mathbf{n}_f$ the wall-normal coordinate, $\delta_f = |\mathbf{x}_f - \mathbf{x}_c|$ the cell-to-face distance and $u_c = \mathbf{u}_c \cdot \mathbf{n}_f$ the wall-normal fluid velocity at cell center. Inserting (53) into (51) yields a second order 'spring-damper' ordinary differential equation for wall-normal droplet position x, to which the well-known solution is given by Longest and Oldham [23]. We can now determine the time t_f at which $x = -d/2$, i.e., the first time at which the droplet intercepts the wall. At this time the 'interception droplet velocity' $v_{i,f}(t_f)$ is computed, and used as the value for $\mathbf{v}_i$ at the wall:

$$\mathbf{v}_i = v_{i,f}(t_f) \mathbf{n}_f. \tag{54}$$

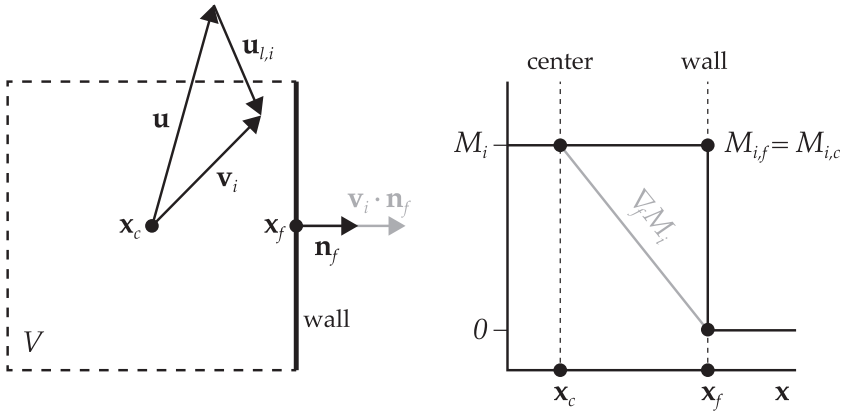

Fig. 1. Left: a schematic overview of a computational volume with a wall face and the velocity boundary conditions. The cell center is located at $\mathbf{x}_c$ and the wall face at $\mathbf{x}_f$. At the cell center the fluid has velocity $\mathbf{u}$ and the droplets of size s_i velocity $\mathbf{v}_i$. The wall has outward unit normal $\mathbf{n}_f$. The wall-inward component of the droplet velocity, $\mathbf{v}_i \cdot \mathbf{n}_f$, is shown in gray. Right: M_i as a function of $\mathbf{x}$ near the wall. For drift the concentration M_i at the wall is approximated as cell-centered value $M_{i,c}$. The gradient $\nabla_f M_i$ at the wall is approximated by the gray line working with $M_i = 0$ at the wall.

Table 1
Chosen numerical schemes for the discretization of the indicated terms.

Term	Scheme	OpenFOAM
∂_t	Implicit Euler [39]	`Euler`
$\mathbf{u}_f$, T_f	Linear upwind scheme	`linearUpwind linear`
$Y_{j,f}$, $Z_{j,f}$, $M_{i,f}$	van Leer limiter [40]	`vanLeer`
$\mathbf{v}_{i,f}$	Upwind	`upwind`
∇ (cell-center gradient)	Central	`linear`
∇^2 (Laplacian)	Central	`linear uncorrected`
∇_f (face-normal gradients)	Central	`uncorrected`

3.3.2. Diffusional deposition

We model a perfectly-absorbing boundary to approximate diffusional deposition. When droplets hit a wall they are absorbed instantly, and removed from the domain. Diffusional deposition, as concluded before, is driven by $\nabla n(s, \mathbf{x}, t) \cdot \mathbf{n}$ being non-zero at the wall. However, in the two previously defined deposition boundary conditions we set $\nabla n(s, \mathbf{x}, t) \cdot \mathbf{n}$ to be zero: the numerical treatment of the drift deposition prevents diffusional deposition. Also at the discrete level we encounter this problem. Fig. 1 (left) sketches the solution of M_i near the wall. At the wall, M_i attains the value of M_i at the cell center, indeed showing no gradient at the wall. However, due to the perfectly absorbing boundary condition, we compute the gradient of M_i at the face *in the diffusion flux* as if M_i is zero at the wall to induce diffusion transport towards the wall. If we retain (50c), then this translates into saying

$$\nabla_f(\rho M_i) = \rho \nabla_f M_i = -\frac{\rho_c M_{i,c}}{\mathbf{x}_f - \mathbf{x}_c} \qquad \text{at} \qquad \mathbf{x}_f, \tag{55}$$

which is also schematically shown in Fig. 1 (left) by the gray line.

Even though the discrete implementations are conflicting, we use (50a) or (54) for the computation of the *drift deposition flux* and (55) for the computation of the *diffusional deposition flux*. This approach was also adopted in the drift flux models of Xi and Longest [36] and Longest and Oldham [23], and proved to be successful.

3.4. Schemes and methods

We implement our model in OpenFOAM, using the compressible PISO (Pressure Implicit with Splitting of Operator) algorithm as documented in [27]. Together with the transport equations for $n(s, \mathbf{x}, t)$ (discretized in terms of M_i), Y_j, Z_j and ρ as presented before, we solve the Navier–Stokes equations for the mixture velocity $\mathbf{u}$ and the energy equation for temperature T, see [27]. In the PISO algorithm the continuity Eq. (15) is rewritten into the pressure equation, using an equation of state, see [37,38]. In OpenFOAM we must select suitable spatial and temporal schemes for the discretization of the equations. Table 1 shows an overview of our choices. All discretization schemes listed in Table 1 are the standard schemes implemented in OpenFOAM.

4. Validation of inertial and diffusion aerosol deposition in bent pipes

In this section, we use our model and method to simulate aerosol droplet deposition in bent pipe geometries. For the description of the bent pipe geometry, Section 4.1, we closely follow the works by the authors in [10,15,20,21], all of which studied inertial deposition in two geometrically different 90° bent pipes, each operated at a different Reynolds number. In this section, we will discuss the bent pipe geometry and study the numerical flow and deposition solutions in terms of temporal and spatial sensitivity. Moreover, in both the diffusional and inertial deposition regime we compare our results against data from literature. Finally, bent pipe deposition for a large range of Reynolds and curvature ratios is shown.

4.1. The bent pipe setup

Fig. 2 shows schematically the bent pipe geometry. In agreement with [15], the inlet of the bent section is extended by a distance D, and the outlet by a distance $2D$, with D the diameter of the pipe, as depicted. We retain this choice in geometry to allow direct comparison with the results of Pilou et al. [15]. Following Pui et al. [21] we set

$$R^\star = \frac{r}{R} \tag{56}$$

Table 2
Simulation parameters for water droplets carried by air at room temperature and atmospheric conditions. The fluid velocity through the pipe is based on the Reynolds number.

Parameter	Value	Unit
μ	1.81×10^{-5}	m^2/s
ρ	1.1898	kg/m^3
ρ^ℓ	10^3	kg/m^3
T_0	293.15	K
$D(Re = 100)$	0.93×10^{-3}	m
$D(Re = 1000)$	0.93×10^{-3}	m
r	$R^\star D/2$	m
U	$Re\,\mu/(\rho D)$	m/s
p_0	10^5	Pa
$\mathbf{g}$	$\mathbf{0}$	m/s^2

as the curvature ratio, i.e., the ratio of bend radius r and pipe radius R defined as $R = D/2$. The Reynolds number is defined as

$$Re = \frac{\rho U D}{\mu}, \tag{57}$$

with bulk velocity U. The Stokes number, expressing the ratio between droplet inertial time scale and the fluid convective time scale, is given by

$$St = \frac{\rho^\ell d^2 U C_c}{18 \mu R}. \tag{58}$$

where ρ^ℓ is the liquid droplet density and d the droplet diameter. Note that the Stokes number is based on R whereas the Reynolds number is based on D, in accordance to [21]. The Peclet number, introduced here for later use, expresses the ratio of convective and diffusive droplet transport. It is defined as

$$Pe = \frac{UD}{\mathbb{D}}, \tag{59}$$

with $\mathbb{D}$ the size-dependent diffusivity, as given by (24). In the bent pipe geometry an important quantity is the Dean number, defined as

$$De = \frac{Re}{\sqrt{R^\star}}. \tag{60}$$

The flow field in bends of circular cross section only depends on this number, expressing the ratio of the centrifugal and inertial forces to the viscous forces.

Table 2 lists all values for the simulation parameters, based on water droplets immersed in air at room temperature T_0 and atmospheric pressure p_0. In all simulations we set the Reynolds number by specifying U, while keeping ρ and μ constant and taking pipe diameter D from [15]. Simulations are essentially governed only by Re and $R^\star$ [41]. We set gravity to zero, such that gravitational settling of droplets is neglected. In [15,20] it was concluded that the effects of gravity were found to be relatively small for the two studied cases in their work. However, in [21] it was concluded that for the $Re = 100$ case the orientation of the bent pipe with respect to gravity had an effect on the deposition results and the experimental reproducibility. Therefore, in the $Re = 100$ case we will also include gravity in our simulations for the inertial deposition validation. This will be clearly indicated.

For the mesh, we apply an 'O-type multiblock structure' as was done in [15]. The pipe cross section contains an internal square of size $D/5$, to avoid very small computational volumes at the pipe centerline, as would appear in a purely cylindrical mesh. The internal square is extended to the pipe wall by an enclosing cylindrical mesh, see Fig. 2 (right). Towards the pipe wall we apply a boundary layer grid refinement, such that in radial direction cells at the wall are a factor 5 smaller than cells at the internal square.

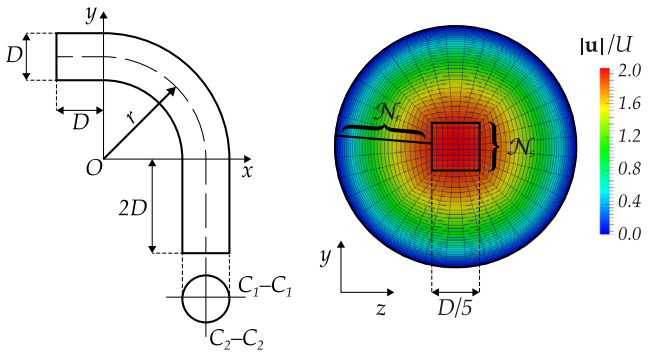

Fig. 2. Left: schematic overview of the bent pipe geometry. The inlet extension has length D, the outlet extension length $2D$, with D the pipe diameter. The bent has radius r. Right: cross section of the O-type mesh, shown for Mesh C, with the internal block of width $D/5$, number of internal square cells $\mathcal{N}_s$ and number of radial cells $\mathcal{N}_r$. The color indicates the magnitude of the parabolic inlet velocity profile.

Table 3
Definition of the used meshes with N_s the number of cells for a side of the internal square, $\mathcal{N}_r$ the number of cells in radial direction, G the linear grading factor in radial direction (indicating the ratio between the smallest and largest cell, with the smallest cell at the wall) and $\mathcal{N}_t$ the total number of computational cells for $R^\star = 7$. The 'no-bl' suffix implies that no grid refinement to the wall is applied, i.e., $G = 1$.

Mesh	$\mathcal{N}_s$	$\mathcal{N}_r$	G	$\mathcal{N}_t$	$\Delta x_c/D$	$\Delta x_w/D$
A-no-bl	5	9	1	41.820	0.04000	0.035858
B-no-bl	7	12	1	104.720	0.02857	0.02988
C-no-bl	9	16	1	234.549	0.02222	0.02241
D-no-bl	11	20	1	459.459	0.01818	0.01792
E-no-bl	14	25	1	922.488	0.01429	0.01434
A	5	20	5	86.700	0.03568	0.007136
B	7	26	5	211.344	0.02752	0.005503
C	9	34	5	465.885	0.02108	0.004217
D	11	44	5	944.163	0.01632	0.003263
E	14	55	5	1.893.528	0.01307	0.002613

We introduce five different grids, A, B, C, D and E, each being a refined version of its parent with A being the coarsest. Also, we define five non-graded grids, identical to the five graded grids but without a boundary layer grid refinement. In the pipe cross section, the mesh is defined by $\mathcal{N}_s$ and $\mathcal{N}_r$, being the number of cells spanning one side of the internal square and the number of cells in radial direction from the internal square to the pipe wall, respectively. These two numbers are also indicated in Fig. 2 (right). Along the pipe axis cells have a uniform spacing, chosen such that their width in axial direction is equal to the width in cross-sectional direction of a cell within the internal square. The number of cells in axial direction is a function of $R^\star$. Table 3 gives the values for $\mathcal{N}_s$, $\mathcal{N}_r$ and $\mathcal{N}_t$ for each grid. The total number of cells, $\mathcal{N}_t$, is indicated in Table 3 for $R^\star = 7$. The meshes are chosen such that $\mathcal{N}_t$ *roughly doubles* from one mesh to the next. This means that the typical cell dimension Δx decreases roughly by a factor $2^{1/3}$. In that sense, Mesh E contains cells only a factor $2^{4/3}$ smaller in typical size with respect to Mesh A.

For the boundary conditions we apply the ones shown in Table 4 for inlet, outlet and wall, in addition to the uncorrected or corrected deposition boundary treatment for inertial deposition and the perfectly absorbing boundary condition in the computation of the diffusion terms. The fluxes for the liquid concentrations follow directly from (11), and are computed explicitly. At time $t = 0$ we start from a quiescent state in which no aerosol is present in the system. We use a distribution of sectional representative sizes s_i which is evenly spaced in $\log d$-space, and ranges from approximately $d = 3$ nm as the smallest size to $d = 20$ µm as the largest

Table 4
List of boundary conditions for each variable and boundary patch. ZG stands for 'zero gradient'.

Variable	Inlet	Outlet	Wall
Z (droplet)	10^{-5}	ZG	ZG
Y (air)	$1-Z$	ZG	ZG
M_i	$\mathcal{M}_0$	ZG	Mixed*
p	ZG	0	ZG
T	293.15	ZG	293.15
$\mathbf{u}$	U**	ZG	0
$\mathbf{v}$	$\mathbf{u}$	(Un)corrected	ZG

* As described in Section 3.3.
** Parabolic velocity profile with its maximum at $2U$ such that the mean bulk flow is U.

size. We set a parabolic inlet velocity profile with its maximum at $2U$, for both $\mathbf{u}$ and $\mathbf{v}_i$. This profile is ramped starting from a quiescent state $\mathbf{u}=0$ over the time interval $t\in[0,\tilde{\tau}]$, with

$$\tilde{\tau}=\frac{L}{U} \tag{61}$$

where L is the centerline length of the pipe. The time $\tilde{\tau}$ is the bulk flow-through time of the system, a quantity which we can use to define the non-dimensional flow-through time $t^\star$ as

$$t^\star=\frac{t}{\tilde{\tau}}. \tag{62}$$

For $t>\tilde{\tau}$ the parabolic inlet fluid and droplet velocity profile remains constant with its maximum at $2U$.

4.2. Flow solution

In the work of Pui et al. [21] inertial deposition of aerosol is experimentally studied using two cases: $Re=100$, $R^\star=7$ and $Re=1000$, $R^\star=5.7$. These two cases were also numerically investigated by Pui et al. [15], Tsai and Pui [10] and Vasquez et al. [20]. We compare our flow solutions against the well-established results of Pilou et al. [15].

Fig. 2(left) shows pipe cross section lines C_1–C_1 and C_2–C_2. Along these two lines we compute the scaled axial velocity magnitude, i.e., $|\mathbf{u}|/U$. Fig. 3 shows this quantity along C_1–C_1 and C_2–C_2 for the bend inlet (I), halfway the pipe bend (H) and at the bend outlet (O) for the $Re=100$ and $Re=1000$ cases, computed on the five refined meshes, A–E. Also, the data of Pilou et al. [15] is shown. For most meshes the results are very similar. Generally, we find good agreement with [15], for all meshes. We see a notable change in the solution towards the literature data for both cases as the mesh is refined. This is in agreement with the observations of [20], where the $Re=100$ solution becomes effectively grid-independent beyond 10^6 cells while the $Re=1000$ solution becomes nearly grid-independent for 3.3×10^6 cells.

In this paper, we are in particular focusing on the accuracy of the solution in terms of the diffusion and inertial deposition. We will present the assessment of the grid dependence of those quantities in the next section. We conclude that our flow predictions agree well with data from literature.

4.3. Convergence of the deposition efficiency

A relevant quantity in the study of aerosol deposition is the *deposition efficiency* η, defined as the ratio of 'that what deposits in the system' over 'that what enters the system'. At the numerical level, we define the deposition efficiency for droplet section i as

$$\eta_i=\frac{\sum_{f\in\mathcal{W}}\Phi_{i,f}}{\sum_{f\in\mathcal{I}}\Phi_{i,f}}, \tag{63}$$

with $\mathcal{W}$ and $\mathcal{I}$ the set of faces belonging to the wall and inlet, respectively, and

$$\Phi_{i,f}=\left(\phi_f+\phi_{i,f}^{\text{drift}}\right)M_{i,f}+\phi_{i,f}^{\text{diff}} \tag{64}$$

the total flux of s_i-sized droplets crossing face f. Note that the fluxes contain the face f surface area through their corresponding definitions (11), such that summing them over the sets $\mathcal{W}$ and $\mathcal{I}$ represents the numerical equivalent of a surface integral. In the sectional formulation we can now, given a sectional distribution spanning some space in s, compute how η depends on the size s.

Fig. 4 (left) shows the logarithm of the deposition efficiency as a function of the logarithm of droplet diameter d. In this log-log space we recover a V-shaped deposition efficiency curve, where the left side of the V is governed by diffusional deposition and the right side by inertial deposition. For small d the droplet diffusivity increases, increasing diffusional deposition in turn. For large d the droplet inertial time scale becomes larger and droplets drift away from the carrier gas trajectory, increasing inertial deposition.

Our time-resolving algorithm allows to obtain η as a transient quantity. It will take some time before η has, given the initial condition of quiescence, converged to its steady state solution. Fig. 4 (left) shows η as a function of d for six non-dimensional flow-through times $t^\star$, computed using Mesh E. As $t^\star$ increases, the η-curves are seen to approach a steady state, for both meshes. Fig. 4 (right) shows how the minimum of the η-curve settles as a function of non-dimensional flow-through time $t^\star$. For the $Re=100$ case, having a smaller Reynolds and Dean number, steady state is only attained around $t^\star=30$, whereas the $Re=1000$ case converges more rapidly. Also, an increase in grid density increases the transient time. This means that if the solution for Mesh E is well-developed, so are the solutions on the coarser meshes, motivating the choice to only show results for Mesh E in Fig. 4. For the 'no-bl' meshes (see Table 3) the transient time amounts to less than 5 flow-through times (not shown in Fig. 4). In the remainder of this paper all presented results are taken at $t^\star=30$, i.e., the bulk flow was allowed to pass the complete length of the pipe 30 times, before recording the steady-state deposition efficiency η. This was found adequate, as at this time all curves in Fig. 4 (right) have become reasonably 'flat', indicating steady state.

Fig. 5 shows, for $Re=100$ and $Re=1000$, the deposition efficiency computed on all five meshes, with or without boundary layer, using the corrected and uncorrected wall velocity boundary treatment. The 'no-bl' meshes produce a deposition efficiency curve very dissimilar to that of the refined meshes with a large grid dependence, clearly indicating the relevance of a boundary layer mesh. Considering the solutions for Mesh A to E, we see that the deposition efficiency is only sensitive to the mesh density in the bottom of the V-shape, where η has dropped to about 10^{-4}. In the diffusion-driven left arm and inertia-driven right arm of the deposition efficiency curve the results are close to grid-independent. The uncorrected boundary condition gives, as expected, a significant overprediction of the deposition efficiency, in particular for the 'no-bl' meshes and for the coarser wall-refined meshes. For the corrected boundary condition the solution is much less grid sensitive, although for the 'no-bl' meshes the deposition efficiency for $Re=1000$ around the bottom of the V varies notably. Both the uncorrected and corrected boundary conditions appear to produce almost the same efficiency curve on the finest mesh E, both for $Re=100$ and $Re=1000$.

To study the grid dependence of the solution quantitatively we introduce the deposition curve integral

$$e=\int_\Omega \log\eta\,\mathrm{d}\log d, \tag{65}$$

in which Ω is the domain in d shown in Fig. 5. This relation is approximated numerically by a simple Riemann sum over all sec-

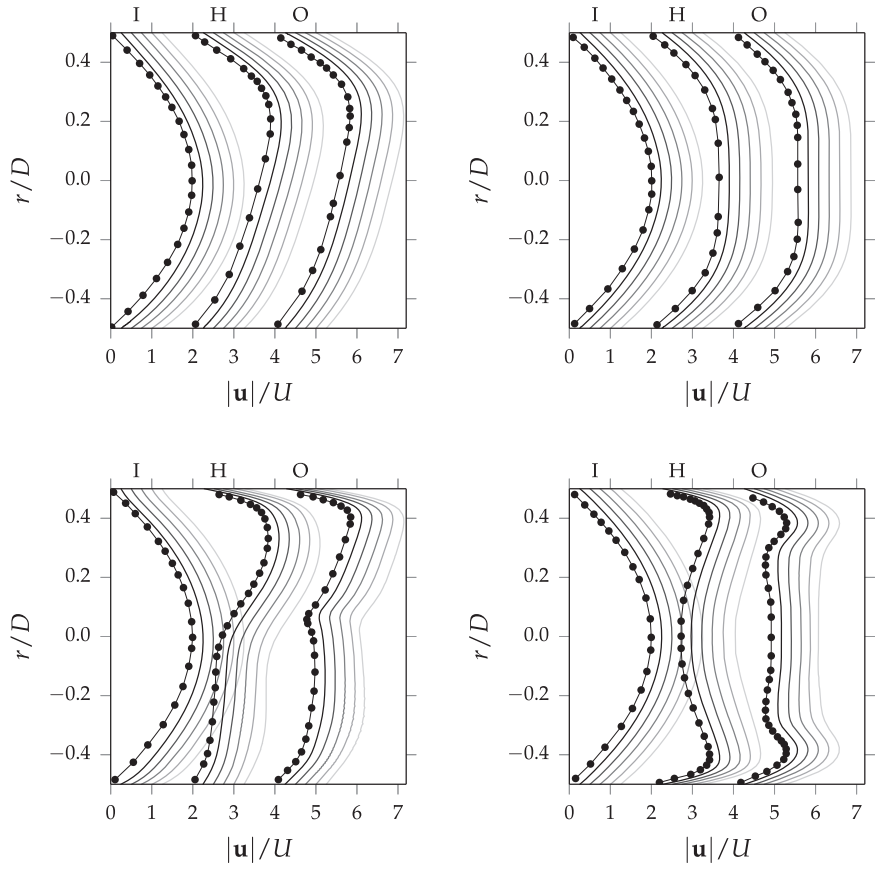

Fig. 3. Bent pipe steady state axial velocity profiles for $Re = 100$ (top row) and $Re = 1000$ (bottom row), along pipe cross sections C_1–C_1 (left column) and C_2–C_2 (right column), at the bend inlet (I), halfway the bend (H) and at the bend outlet (O), each horizontally offset by 2 for better visibility of the profiles. From gray to black (—) mesh A–E are shown. The cross sections C_1–C_1 and C_2–C_2 are defined in Fig. 2 (left). The data of Pilou et al. [15] (•) is also shown.

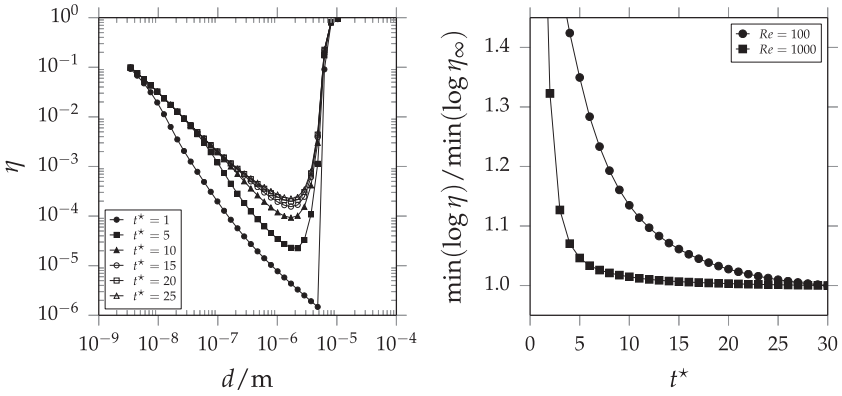

Fig. 4. Left: the $Re = 100$ deposition efficiency η for a range of droplet diameters d, shown at six non-dimensional flow-through times (as indicated) for Mesh E. Right: the convergence of the scaled minimum of the logarithm of η in time, for $Re = 100$ (•) and $Re = 1000$ (■), computed on mesh E. The value for η_∞ is taken at $t^* = 30$. Both figures contain results using the uncorrected boundary treatment.

tions. Table 5 gives e for the five meshes. Also shown in this table is convergence measure Δe, defined as:

$$\Delta e^2 = \int_\Omega (\log \eta - \log \eta_{\text{parent}})^2 \, \mathrm{d} \log d \tag{66}$$

where η_{parent} belongs to the coarser parent mesh. Δe indicates how, with each refinement step, the solution changes in log-space. Generally, for finer meshes it is shown that Δe becomes smaller in both the $Re = 100$ and $Re = 1000$ case, for both boundary conditions, indicating that the solution converges. This information can also be visually distilled from Fig. 5 where the lines for Mesh D and E are closer to each other than those of Mesh A and B.

Fig. 6 shows scaled deposition curve integral e/e_{ref} as function of Δx_w as given by Table 3. The reference value e_{ref} is taken as e for the uncorrected simulation with boundary refinement on Mesh E. From Mesh A to E Δx_w decreases roughly one decade. The quantity e appears to convergence to unity as Δx_w becomes smaller, since the curves appear to become flatter for small Δx_w.

Figs. 5 and 6 and Table 5 indicate that in most practical cases a computation performed on the refined Mesh A using the corrected boundary condition gives a numerically adequate estimate of the deposition efficiency in the diffusion, intermediate (i.e., the bottom of the deposition curve) and inertial regime, which is already within 10% of the deposition curve computed on the refined Mesh E. Having established an impression of the numerical robustness of the solution in terms of the velocity field and deposition efficiency both as a function of grid density, the question remains how phys-

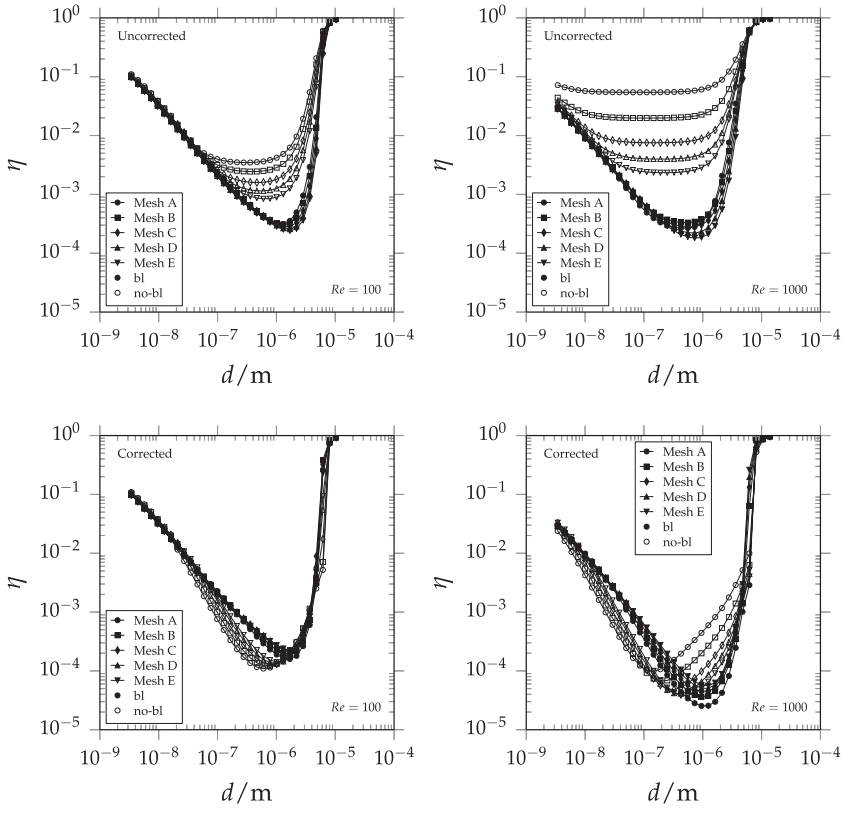

Fig. 5. The grid dependence of the η-curve for $Re = 100$ (left) and $Re = 1000$ (right), for all meshes as defined by Table 3, using the uncorrected boundary condition (top) and corrected boundary condition (bottom).

Table 5
Deposition curve integral e, Eq. (65), and convergence measure Δe, Eq. (66), for $Re = 100$ and $Re = 1000$, uncorrected and corrected deposition velocity and for all five meshes.

	Uncorrected				Corrected			
	$Re = 100$		$Re = 1000$		$Re = 100$		$Re = 1000$	
Mesh	e	Δe	e	Δe	e	Δe	e	Δe
A	−8.0321		−8.6685		−8.2704		−9.7996	
B	−8.1047	0.1003	−8.6045	0.1311	−8.2500	0.1027	−9.5519	0.4312
C	−8.2084	0.1039	−8.7509	0.1261	−8.2710	0.1101	−9.5210	0.1603
D	−8.3003	0.0862	−8.9282	0.1393	−8.3223	0.0632	−9.5393	0.1117
E	−8.3676	0.0613	−9.0832	0.1235	−8.3749	0.0515	−9.5682	0.0822
A-no-bl	−6.3214		−3.7847		−7.7941		−7.0371	
B-no-bl	−6.6076	0.2059	−5.0040	0.6980	−7.8413	0.1403	−7.8298	0.4130
C-no-bl	−6.9363	0.2355	−6.0595	0.6248	−7.9229	0.1646	−8.4605	0.3314
D-no-bl	−7.1788	0.1788	−6.6810	0.3861	−7.9759	0.1648	−8.8041	0.1944
E-no-bl	−7.3997	0.1689	−7.1492	0.3029	−8.0362	0.1073	−9.0306	0.1420

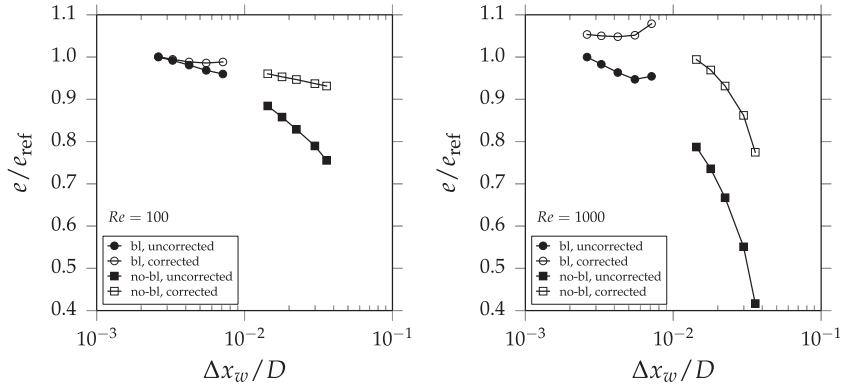

Fig. 6. Deposition curve integral e, Eq. (65), as function of the typical scaled wall grid cell size $\Delta x_w/D$, for $Re = 100$ (left) and $Re = 1000$ (right), with (○, •) and without (□, ■) boundary layer and with the corrected (○, □) and uncorrected (•, ■) boundary treatment for the droplet wall velocity.

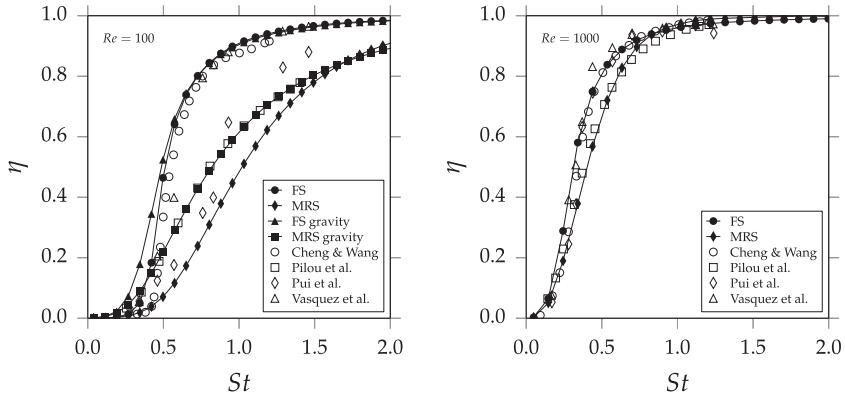

Fig. 7. Inertial deposition efficiency as a function of St for $Re = 100$ (left) and $Re = 1000$ (right), computed on Mesh C using the uncorrected droplet velocity boundary condition and the 'Full Stokes' model (●), 'Full Stokes' with gravity (■) and 'Manninen's reduced Stokes' model [32] (◆). Also shown are the predictions of Cheng and Wang [8] (○), Pilou et al. [15] (□), Pui et al. [21] (◇) and Vasquez et al. [20] (△).

ically accurate the deposition predictions are. We will address this question next by investigating the inertial and diffusional deposition contributions.

4.4. Inertial deposition

On the 'inertial side' of the deposition efficiency curve much research is already available in literature. Cheng and Wang [8] investigated numerically the inertial deposition of aerosol based on an analytical approximation of the fluid velocity in a bent pipe. Pui et al. [21] presented experimental results, whereas Pilou et al. [15] and Vasquez et al. [20] published numerical deposition data. Fig. 7 shows our predictions in comparison with data of aforementioned authors, computed on mesh A using the uncorrected boundary condition. In the inertial regime Mesh A already produced sufficiently grid-independent results and is therefore the only mesh shown in Fig. 7. For both $Re = 100$ and $Re = 1000$ we see good agreement with [8,20]. Vasquez et al. [20] also adopted an Eulerian aerosol model and solved the Eulerian equations for the droplet velocity $\mathbf{v}$ (here referred to as 'Full Stokes' (FS)) without introducing the *local equilibrium approximation*. Good agreement of our predictions is therefore expected. Pilou et al. [15] also model the aerosol drift in an Eulerian setting, but implement the local equilibrium approximation for $\mathbf{v}$ (here referred to as 'Manninen's Reduced Stokes' (MRS) model [32]) and include gravity. Our MRS predictions including gravity lay close to those of [15] for both $Re = 100$ and $Re = 1000$. For the $Re = 1000$ case our results including gravity are not shown as they lie very close to the curves without gravity. Note that for the $Re = 100$ case gravity points in the axial inlet direction while for the $Re = 1000$ case gravity points in the axial outlet direction, see [21]. In the $Re = 100$ case, for the FS model the influence of gravity is small, as was also shown in [20]. For $Re = 100$ our data shows a notable difference with the experimental data of Pui et al. [21]. However, we have an excellent agreement with the model of [8] and the numerical results of [20]. In particular, the agreement with [20] underpins our model and method which are closely related. The difference with the experimental data of Pui et al. [21] remains unexplained. For $Re = 1000$ the agreement is much better. In general we conclude from Fig. 7 that our predictions correspond well to the range of literature data.

4.5. Diffusional deposition

For small Reynolds numbers or large curvature ratios (i.e., De is small), the flow through a smoothly bent pipe is very similar to the flow through a straight pipe. Fig. 3 illustrate this well; the $Re = 100$ velocity solutions resemble more closely the symmetric parabolic Poiseuille flow profile than those for $Re = 1000$. In the limit of $Re \to 0$ or $R^\star \to \infty$ (provided that the flow remains laminar) the aerosol diffusional deposition reduces to its straight pipe solution of equivalent pipe length. Ingham [28] studied this problem and found a convenient analytical expression approximating the cross section averaged aerosol concentration as a function of Pe and pipe length, given a uniform inlet aerosol concentration and developed parabolic velocity profile. Ingham's expression, in terms of η, Pe and pipe length L, is given by the series

$$\eta_I = 1 - \sum_k \alpha_k \exp\left(-\beta_k \left[\frac{\delta}{Pe}\right]^{\gamma_k}\right), \tag{67}$$

with $\delta = L/D$ the ratio between axial pipe length L and the pipe diameter, and coefficients α_k, β_k and γ_k given by Ingham [28]. This η gives a prediction of the diffusional deposition efficiency of a straight pipe. Ingham gives an approximate expression retaining only 4 terms and shows that this is of good accuracy. In arriving at this result it is assumed that droplet diffusion in axial direction can be neglected. This assumption is valid for $Pe \gg 1$ [28], i.e., when convective transport dominates diffusive transport. Therefore, we expect that for small Pe, i.e., for small droplets, the Ingham equation becomes less reliable.

Fig. 8 shows the deposition efficiency, for $Re = 100$ and $Re = 1000$, and for a straight pipe with axial length equal to that of the $Re = 100$ or $Re = 1000$ bent pipe geometry operated at equal conditions. A good agreement is shown between Ingham's model and the straight pipe solution. For $d < 10$ nm our predictions slowly deviate from Ingham as Pe starts to approaches unity. We see that for all displayed d there is a deposition efficiency *enhancement* for the bent pipe case with respect to the straight pipe solution which appears to be quite uniform in d. This enhancement becomes more pronounced as Re (or De) increase. We identify two possible mechanisms driving this enhancement:

1. Fig. 3 shows that the fluid is 'pushed' towards the outer edge of the bend where, in comparison with a straight pipe, more surface is available to deposit, increasing the diffusional deposition flux.
2. Due to the bulk of the flow being pushed towards the outer edge, the perfectly absorbing boundary condition may induce a sharper gradient in comparison with the straight pipe solution, also increasing the diffusional deposition flux.

We conclude that in the range of validity of Ingham's model, we find good agreement with our numerical predictions of the straight pipe flow. For the bent pipe there is an increase in diffusion-driven deposition. An interesting question that arises is how this deposition enhancement depends on the characteristics of the bent pipe flow, as expressed by De, or Re and $R^\star$. We turn to this next.

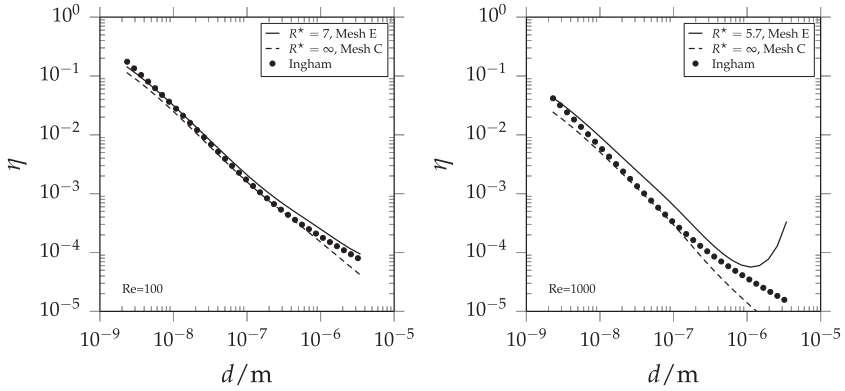

Fig. 8. As a function of d the diffusional deposition for $Re = 100$ (left) and $Re = 1000$ (right), computed on Mesh E (—). Also shown is the model of Ingham (•) and simulated deposition efficiency results for $R^\star = \infty$ (– – –) i.e., a straight pipe, with a mesh equivalent to that of C. The gray area marks the region in between the bent and straight pipe solutions.

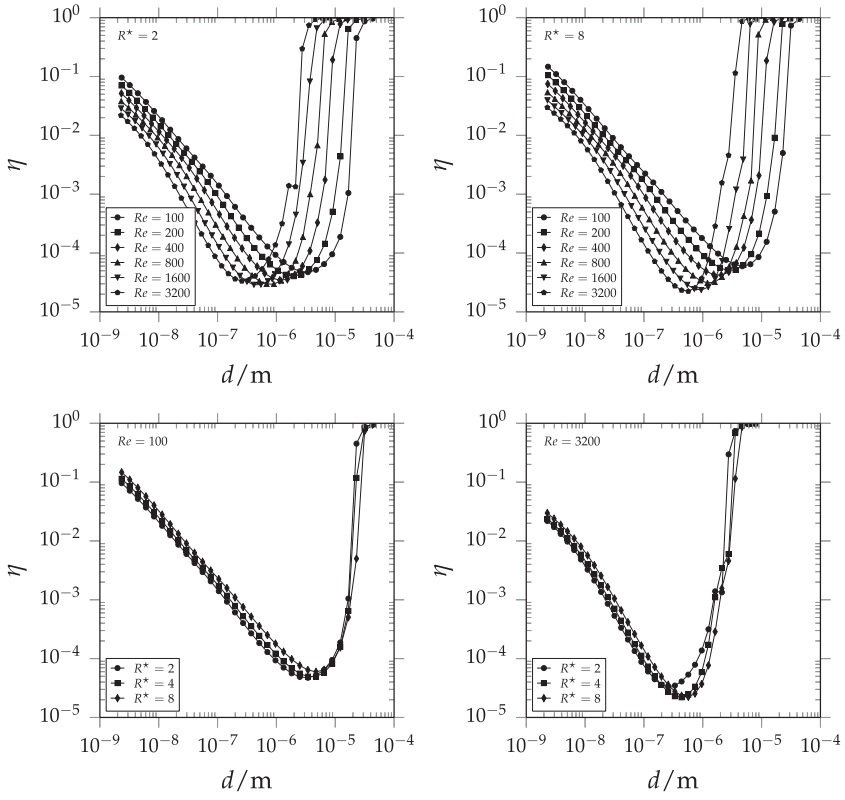

Fig. 9. Deposition curves computed on Mesh A for a range of Re with constant $R^\star$ as indicated (top row) and for a range $R^\star$ with constant Re as indicated (bottom row).

4.6. Re *and* R**-dependence*

Even though we see a strong grid dependence of the solution of $\log \eta$, the solution is sufficiently robust to investigate qualitative changes in the solution as the parameters of the bent pipe change. We identify Re and $R^\star$ as two such parameters, which we vary by setting U and r, respectively. Our model is unique as it allows predictions of both the diffusive and the inertial range within one approach. Intuitively speaking, increasing Re makes the flow more small-scale but also reduces the flow-through time. On the other hand, increasing $R^\star$ makes the bend more gradual but also increases the flow-through time. These are opposing trends that we quantify next. Fig. 9 shows the deposition efficiency for a range of Re and $R^\star$, as indicated, computed on the wall-refined Mesh A using the corrected droplet velocity boundary condition.

In Fig. 9 (top row) $R^\star$ is kept constant at 2 or 8, while Re is varied. On the inertial side of the curve we see a clear increase of η. For example, at $d = 4$ µm we see an increase of four decades in η from $Re = 100$ to $Re = 3200$. In the diffusion regime for constant d the deposition efficiency decreases with increasing Re. From $Re = 100$ to $Re = 3200$ the deposition efficiency, for the smallest shown droplet diameter, decreases roughly by a factor 5, for both values of $R^\star$. However, the residence time decreases by a factor 32. This indicates that as Re increases, the diffusional deposition is enhanced. This was also shown in Fig. 8.

For the results shown in Fig. 9 (bottom row) the Reynolds number is kept constant at 100 or 3200, and $R^\star$ is varied. In general, the deposition curve is not very sensitive to the shown changes in $R^\star$. An enhancement in the inertial regime is shown as $R^\star$ decreases while in the diffusion regime an enhancement is shown as $R^\star$ increases, due to a larger droplet residence time. In general, the effect of Reynolds number on the deposition efficiency is more pronounced than the effect of the curvature ratio on the deposition efficiency. This is also observed in [15,42].

5. Conclusions

In this paper, we presented a compressible Eulerian internally mixed sectional aerosol model. We incorporated droplet drift and droplet diffusion, in turn driving droplet deposition. We proposed two boundary treatments for the sectional droplet number concentrations and drift velocity, to enable both diffusion and inertial deposition. We introduced the uncorrected zero-gradient boundary condition for the droplet velocity, and the corrected one, based on the work of Longest and Oldham [23]. We validated the model by means of simulation of bent pipe deposition. We found a numerically reliable solution on meshes with wall refinement while using the corrected droplet velocity boundary condition. In both the diffusion and inertial regime we identified clear trends which agreed well with literature.

The sectional formulation was shown to have the ability to model a polydisperse aerosol without requiring any assumption on the shape or moments of the size distribution. We specified a uniform distribution (uniform with respect to the sectional concentrations M_i) spanning a droplet diameter domain of $2 \times 10^{-3} \leq d \leq 5 \times 10^{1}$ µm where the representative sectional sizes where uniformly distributed in $\log d$-space. In a single simulation the deposition patterns and efficiencies were computed for this complete droplet size domain, resulting in deposition efficiency curves as a function of $R^\star$ and Re. This feature makes the method extremely useful in modeling of polydisperse aerosols.

To validate the method, we compared against experimental and numerical data from literature for inertial deposition in a bent pipe geometry for two Reynolds numbers and bent radii. Generally, we found good agreement with the numerical predictions of [8,20], where, for the latter case, the 'Full Stokes' (FS) Eulerian equation of motion for droplet velocity was solved, as was done in our work. When employing the 'Manninen Reduced Stokes' (MRS) model in the prediction of particle velocities we saw, for the low Reynolds case $Re = 100$ and $St > 0.1$, a significant deviation from both experimental and numerical data from literature. Also for the $Re = 1000$ case we saw a smaller but notable difference. This encourages the choice for solving the full droplet equation of motion, instead of a simplified model as was done in for example [15].

Our approach showed very good agreement to the analytical aerosol diffusion model of [28] when applied to a straight pipe. Only for very small droplets, where the Peclet number becomes smaller, a deviation from theory was shown. This is to be expected, since the analytical solution for pipe diffusional deposition is no longer valid there.

Having validated both deposition regimes, finally, we tested the dependence of the deposition curve on the Reynolds number Re and curvature ratio number $R^\star$. We used relatively coarse meshes and discussed only qualitative trends. When increasing Re we saw deposition enhancement. Also, a larger Re was shown to lead to a significant increase in inertial deposition. a ten-fold increase in Re leads, for $d = 4$ µm, to a deposition enhancement of roughly four order of magnitude. The increase in $R^\star$ was such that the pipe length increases as well. This means that, at constant flow rate, the droplets have more time to diffuse, indeed increasing deposition in the diffusion regime slightly. In the inertial regime we saw a small increase as $R^\star$ becomes larger.

Acknowledgments

The research presented in this work was funded by Philip Morris Products S.A. (part of Philip Morris International group of companies).

Appendix A. List of symbols

- In the appendix of the manuscript the following table is added:

Variable	Description	Unit
s	Droplet size	kg
$\mathbf{x}$	Position	m
t	Time	s
$\tilde{\tau}$	Bulk flow-through time	s
τ	Droplet relaxation time	s
n	Droplet size distribution	$1/(\text{kg m}^3)$
$\mathbf{u}$	Mixture velocity	m/s
$\mathbf{v}$	Droplet velocity	m/s
$\mathbf{u}^\ell$	Drift velocity	m/s
$\mathbb{D}$	Diffusivity	m^2/s
Y	Vapor mass fraction	dimensionless
Z	Liquid mass fraction	dimensionless
ρ	Mass density	kg/m^3
p	Pressure	Pa
ψ, χ	Compressibility ratio	$\text{kg/(m}^3\text{Pa)}$
$\mathbf{f}$, $\mathbf{h}$	Flux	$\text{kg/(m}^2\text{s)}$
k_B	Boltzmann constant	$\text{m}^2\text{kg/(s}^2\text{K)}$
T	Temperature	K
C_c	Cunningham correction factor	dimensionless
μ	Viscosity	kg/(m s)
d	Droplet diameter	m
λ	Mean free path	m
N	Droplet number concentration	$1/\text{m}^3$
M	Droplet number concentration	$1/\text{kg}^3$
ϕ	Convective face flux	kg/s
ϕ^{drift}	Drift face flux	kg/s
ϕ^ℓ	Total liquid face flux	kg/s
ϕ^{diff}	Diffusion face flux	1/s
Φ	Deposition face flux	1/s
θ	Vapor-to-liquid density ratio	dimensionless
A	Face surface area	m^2
$\mathbf{A}$	Face normal surface area	m^2
$\mathbf{n}$	Face normal	dimensionless
v	Wall-normal droplet velocity	m/s
u	Wall-normal mixture velocity	m/s
x	Wall-normal coordinate	m
δ	Cell-to-face distance	m
U	Bulk velocity magnitude	m/s
D	Pipe inner diameter	m
r	Bend radius	m
R	Pipe inner radius	m
$\mathbf{g}$	Gravity vector	m/s^2
η	Deposition efficiency	dimensionless
$\mathcal{W}$	Set of wall faces	dimensionless
$\mathcal{I}$	Set of inlet faces	dimensionless
e	Deposition curve integral	log m
Δe	Convergence measure	$\log^2$ m
Δx	Cell size	m
$R^\star$	Curvature ratio	dimensionless
Re	Reynolds number	dimensionless
St	Stokes number	dimensionless
Pe	Peclet number	dimensionless
De	Dean number	dimensionless
$t^\star$	Non-dimensional flow-through time	dimensionless
$_c$	Cell index	dimensionless
$_f$	Face index	dimensionless
$_i$	Section index	dimensionless
$_j$	Species index	dimensionless
∂_t	Partial time derivative	1/s
$\nabla\cdot$	Divergence operator	1/m
∇	Gradient operator	1/m

References

[1] Hinds W. Aerosol technology. 2nd. John Wiley & Sons, Inc.; 1999.
[2] Heyder J, Gebhart J, Rudolf G, Schiller C, Stahlhofen W. Deposition of particles in the human respiratory tract in the size range 0.005–15 µm. J Aerosol Sci 1986;17(5):811–25.
[3] Mitsakou C, Helmis C, Housiadas C. Eulerian modelling of lung deposition with sectional representation of aerosol dynamics. J Aerosol Sci 2005;36(1):75–94.
[4] Worth Longest P, Holbrook LT. In silico models of aerosol delivery to the respiratory tract – development and applications. Adv Drug Deliv Rev 2012;64(4):296–311.

[5] Gupta D, Peters M. A Brownian dynamics simulation of aerosol deposition onto spherical collectors. J Colloid Interface Sci 1985;104(2):375–89.
[6] Mora JFDL, Rosner D. Effects of inertia on the diffusional deposition of small particles to spheres and cylinders at low Reynolds numbers. J Fluid Mech 1982;125:379–95.
[7] Zhang Y, Finlay W, Matida E. Particle deposition measurements and numerical simulation in a highly idealized mouth–throat. J Aerosol Sci 2004;35(7):789–803.
[8] Cheng YS, Wang CS. Motion of particles in bends of circular pipes. Atmos Environ (1967) 1981;15(3):301–6.
[9] Crane RI, Evans RL. Inertial deposition of particles in a bent pipe. J Aerosol Sci 1977;8(3):161–70.
[10] Tsai C, Pui D. Numerical study of particle deposition in bends of a circular cross-section-laminar flow regime. Aerosol Sci Technol 1990;12(4):813–31.
[11] Sun K, Lu L, Jiang H. A computational investigation of particle distribution and deposition in a 90° bend incorporating a particle–wall model. Build Environ 2011;46(6):1251–62.
[12] Wilson S, Liu Y, Matida E, Johnson M. Aerosol deposition measurements as a function of Reynolds number for turbulent flow in a ninety-degree pipe bend. Aerosol Sci Technol 2011;45(3):364–75.
[13] Zhang P, Roberts R, Bénard A. Computational guidelines and an empirical model for particle deposition in curved pipes using an Eulerian–Lagrangian approach. J Aerosol Sci 2012;53:1–20.
[14] Breuer M, Baytekin H, Matida E. Prediction of aerosol deposition in bends using LES and an efficient lagrangian tracking method. J Aerosol Sci 2006;37(11):1407–28.
[15] Pilou M, Tsangaris S, Neofytou P, Housiadas C, Drossinos Y. Inertial particle deposition in a 90° laminar flow bend: an Eulerian fluid particle approach. Aerosol Sci Technol 2011;45(11):1376–87.
[16] Armand P, Boulaud D, Pourprix M, Vendel J. Two-fluid modeling of aerosol transport in laminar and turbulent flows. J Aerosol Sci 1998;29(8):961–83.
[17] Mohanarangam K, Tian Z, Tu J. Numerical simulation of turbulent gas–particle flow in a 90° bend: Eulerian–Eulerian approach. Comput Chem Eng 2008;32(3):561–71.
[18] Zhang P, Roberts R, Bénard A. Numerical simulation of turbulent mist flows with liquid film formation in curved pipes using an Eulerian–Eulerian method. J Fluids Eng 2013;135(9): 091303-1–091303-10.
[19] Lin J, Yin Z, Lin P, Yu M, Ku X. Distribution and penetration efficiency of nanoparticles between 8–550 nm in pipe bends under laminar and turbulent flow conditions. Int J Heat Mass Transf 2015;85:61–70.
[20] Vasquez E, Walters K, Walters D. Analysis of particle transport and deposition of micron-sized particles in a 90° bend using a two-fluid Eulerian–Eulerian approach. Aerosol Sci Technol 2015;49(9):692–704.
[21] Pui D, Romay-Novas F, Liu B. Experimental study of particle deposition in bends of circular cross section. Aerosol Sci Technol 1987;7(3):301–15.
[22] Sun K, Lu L. Particle flow behavior of distribution and deposition throughout 90° bends: analysis of influencing factors. J Aerosol Sci 2013;65:26–41.
[23] Worth Longest P, Oldham M. Numerical and experimental deposition of fine respiratory aerosols: development of a two-phase drift flux model with near-wall velocity corrections. J Aerosol Sci 2008;39(1):48–70.
[24] Xi J, Worth Longest P. Transport and deposition of micro-aerosols in realistic and simplified models of the oral airway. Ann Biomed Eng 2007;35(4):560–81.
[25] Frederix E, Stanic M, Kuczaj A, Nordlund M, Geurts B. Characteristics-based sectional modeling of aerosol nucleation and condensation. J Comput Phys 2016;326:499—515.
[26] Frederix E, Stanic M, Kuczaj A, Nordlund M, Veldman A, Geurts B. Application of the characteristics-based sectional method to spatially varying aerosol formation and transport. J Aerosol Sci 2017;104:123–40.
[27] Frederix E, Stanic M, Kuczaj A, Nordlund M, Geurts B. Extension of the compressible PISO algorithm to single-species aerosol formation and transport. Int J Multiphase Flow 2015;74:184–94.
[28] Ingham D. Diffusion of aerosols from a stream flowing through a cylindrical tube. J Aerosol Sci 1975;6(2):125–32.
[29] Kumar S, Ramkrishna D. On the solution of population balance equations by discretization – I. A fixed pivot technique. Chem Eng Sci 1996;51(8):1311–32.
[30] Friedlander S. Smoke, dust, and haze: fundamentals of aerosol dynamics. 2nd. Oxford University Press; 2000.
[31] Walas S. Phase equilibria in chemical engineering. Butterworth-Heinemann; 1985.
[32] Manninen M, Taivassalo V, Kallio S. On the mixture model for multiphase flow. VTT Publications 288, Technical Research Center of Finland; 1996.
[33] Armenio V, Fiorotto V. The importance of the forces acting on particles in turbulent flows. Phys Fluids 2001;13(8):2437–40.
[34] Clift R, Grace J, Weber M. Bubbles, drops and particles. Academic Press; 1978.
[35] Harten A. High resolution schemes for hyperbolic conservation laws. J Comput Phys 1983;49(3):357–93.
[36] Xi J, Worth Longest P. Numerical predictions of submicrometer aerosol deposition in the nasal cavity using a novel drift flux approach. Int J Heat Mass Transf 2008;51(23–24):5562–77.
[37] Issa R. Solution of the implicitly discretised fluid flow equations by operator-splitting. J Comput Phys 1986;62(1):40–65.
[38] Issa R, Ahmadi-Befrui B, Beshay K, Gosman A. Solution of the implicitly discretised reacting flow equations by operator-splitting. J Comput Phys 1991;93(2):388–410.
[39] Morton K, Mayers D. Numerical solution of partial differential equations. Cambridge University Press; 2005.
[40] van Leer B. Towards the ultimate conservative difference scheme: V. A second-order sequel to Godunov's method. J Comput Phys 1979;32(1):101–36.
[41] Brockmann J. Aerosol measurement: principles, techniques, and applications. 3rd. John Wiley & Sons, Inc.; 2011.
[42] Pilou M. Investigation of interactions between particles and flowing biofluids. National Technical University of Athens; 2012.